

Observation of the Inverse Giant Piezoresistance Effect in Silicon Nanomembranes Probed by Ultrafast Terahertz Spectroscopy

Houk Jang,^{†,‡,⊥} Jaeseok Kim,^{†,⊥} Min-Seok Kim,[§] Jeong Ho Cho,^{‡,||} Hyunyong Choi,^{*,†} and Jong-Hyun Ahn^{*,†}

[†]School of Electrical and Electronic Engineering, Yonsei University, Seoul, 120-749, Republic of Korea

[‡]SKKU Advanced Institute of Nanotechnology (SAINT), Sungkyunkwan University, Suwon, 440-746, Republic of Korea

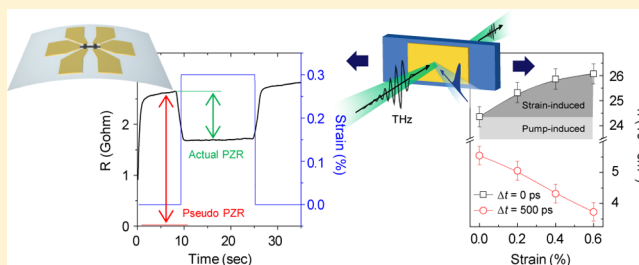
[§]Center for Mass Related Quantities, Korea Research Institute of Standards and Science, Daejeon, 305-340, Republic of Korea

^{||}School of Chemical Engineering, Sungkyunkwan University, Suwon, 440-746, Republic of Korea

Supporting Information

ABSTRACT: The anomalous piezoresistance (a-PZR) effects, including giant PZR (GPZR) with large magnitude and inverse PZR of opposite, have exciting technological potentials for their integration into novel nanoelectromechanical systems. However, the nature of a-PZR effect and the associated kinetics have not been clearly determined yet. Even further, there are intense research debates whether the a-PZR effect actually exists or not; although numerous investigations have been conducted, the origin of the effect has not been clearly understood. This paper shows the existence of a-PZR and provides direct experimental evidence through the performance of well-established electrical measurements and terahertz spectroscopy on silicon nanomembranes (Si NMs). The clear inverse PZR behavior was observed in the Si NMs when the thickness was less than 40 nm and the magnitude of the PZR response linearly increased with the decreasing thickness. Observations combined with electrical and optical measurements strongly corroborate that the a-PZR effect originates from the carrier concentration changes via charge carrier trapping into strain-induced defect states.

KEYWORDS: Inverse piezoresistance effect, ultrathin silicon nanomembrane, defect trapping, ultrafast terahertz spectroscopy



For the previous ten years, there have been intensive studies on silicon (Si), one of the most studied and commercially significant materials, to achieve a breakthrough to integrate Si into flexible electronics by reducing its dimensions in the shape/size/form of nanostructure such as nanomembranes (NMs). Because the thinner Si NMs provide better electrical stability under bending, Si NMs with a thickness of less than 100 nm have been largely used in flexible electronics.^{1,2} Because of the unavailability of mechanical deformation in flexible electronics, it is critical to understand and predict the electromechanical properties of Si NMs. However, when it comes to the nanostructure of Si, a critical controversy on the electromechanical properties is inevitable; the debate of whether the piezoresistance (PZR) behavior, the electrical resistance change under mechanical deformation, in Si nanostructure is different from that of bulk or not is at the heart of the debate. He et al. has reported about the giant PZR (GPZR) in silicon nanowire with orders of magnitude larger than that of bulk Si.³ However, Rowe et al. and Milne et al. have found that the GPZR effect arises from the nonstress related drift of conductance induced by dielectric relaxation of the Si surface, not from the mechanical deformation.^{4,5} Moreover, the authors have insisted that the PZR behavior in nanostructures of Si is not different from that of bulk Si by distinguishing real/

actual PZR, the PZR effect attributed to the mechanical deformation, from the pseudo PZR, the PZR effect from the dielectric relaxation of the Si surface. Recently, Yang et al. have reported about the inverse PZR in which the researchers show an opposite PZR response with increasing magnitude in a thinner or smaller nanostructure compared to that of bulk Si.^{6,7} However, these researchers are also not free from the same argument that has been raised for the GPZR, whether it originates from the mechanical deformation or nonstress related drift of conductance.⁸

This paper provides clear experimental evidence uncovering the mechanism for the inverse PZR. The optically induced conductivity is directly determined under strain via ultrafast terahertz (THz) spectroscopy, which also enables the performance of the in situ analysis of mobility and carrier concentration/density on an equal footing. This observation of the inverse PZR in Si NMs with a thickness of less than 40 nm corroborates that the inverse PZR is the actual PZR whose physical origin arises from the mechanical deformation, not from the pseudo PZR (nonstress related drift of conductance).

Received: August 19, 2014

Revised: October 23, 2014

Published: November 6, 2014

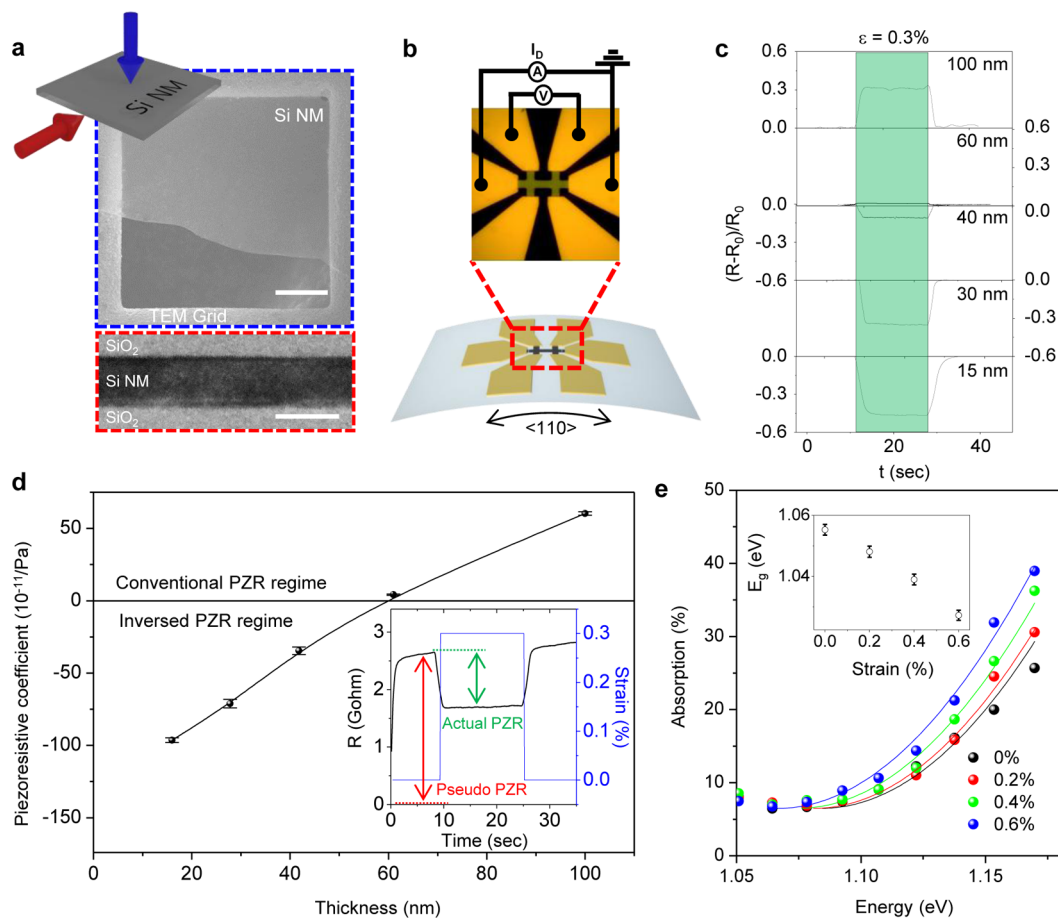


Figure 1. PZR effect in Si NMs investigated by electrical resistance measurement and optical absorption measurement (a) SEM image (upper, scale bar: $10\ \mu\text{m}$) and TEM image (bottom, scale bar: $20\ \text{nm}$) of the representative Si NMs with a thickness of $16\ \text{nm}$. (b) The schematic illustration and optical microscope image of the fabricated device and measurement system. The devices were formed in hall-bar structure and measured by the four-probe system. (c) The measured resistance with the stepped tensile strain of 0.3% (green region) with various thicknesses from 16 to $100\ \text{nm}$ as a function of time, normalized by the resistance without applying strain. (d) The piezoresistance coefficient of the Si NMs as a function of thickness under the tensile strain of 0.3% . The error bars indicate the distribution of PZR coefficient that arises from the drift of resistance during measurement. The inset shows measured resistance of the $30\ \text{nm}$ thick Si NM at the constant current of $1\ \text{nA}$, as a function of time (black) with a stepped tensile strain (blue). (e) The optical absorption of the Si NM with a thickness of $30\ \text{nm}$ near the band edge, $\sim 1.1\ \text{eV}$ under various tensile strain from 0 (black) to 0.6% (blue). The inset shows the fitted average value of E_g (black circle) and standard deviation (error bar) as a function of tensile strain.

Moreover, it was noted that the electrical response in inverse PZR results from the strain-induced change in carrier density at the surface of Si NMs, which definitely differs from the PZR in bulk Si that results from the strain-induced change in mobility.^{9,10} The spectrally and temporally resolved THz responses have evidenced that the strain-induced defect-state indeed plays a prominent role in the generation of additional carrier and that the effect is highly dependent on the surface state of the Si NMs.^{11–13}

Results and Discussion. The inverse PZR in Si NM was studied by fabricating a Si strain sensor on a polyethylene terephthalate (PET) substrate. Figure 1a shows scanning electron microscope (SEM) and transmission electron microscope (TEM) image of the representative Si NMs with a thickness of $16\ \text{nm}$ on TEM grid, confirming its thickness and uniformity over $40\ \mu\text{m}$. The schematic illustration and optical microscope image of the fabricated device are shown in Figure 1b. During the fabrication, experimental variables, such as the doping concentration of $\sim 10^{17}$, direction of the tensile strain along $\langle 110 \rangle$, surface crystal orientation of (100) , and the ohmic contact between the semiconductor and metal electrodes were

carefully controlled. The detailed description of the fabrication process is described in the Supporting Information Figure S1. The PZR behavior of the Si NMs with varying thicknesses from 16 to $100\ \text{nm}$ was investigated by measuring the resistance of the fabricated Si strain gauges in time with the stepped tensile strain of 0.3% , which corresponds to tensile stress of $5.1\ \text{GPa}$ as shown in Figure 1c. The mechanical deformation, defined as a value of strain, was well controlled by bending the strain gauge using micromanipulator with a step motor, and the corresponding strain values were calculated based on the multilayer bending model with parameters shown in Supporting Information Table S1, as previously reported.¹⁴ The measured PZR coefficients, summarized in Figure 1d, are defined by the following equation

$$\text{Piezoresistance coefficient} = \frac{R - R_0}{R_0 \cdot \sigma} \quad (1)$$

where R is the resistance under strain, R_0 is the resistance without strain, and σ is the applied stress. By decreasing the thicknesses of Si NMs, a significant change of the PZR coefficient was observed in both magnitude and sign. The 100

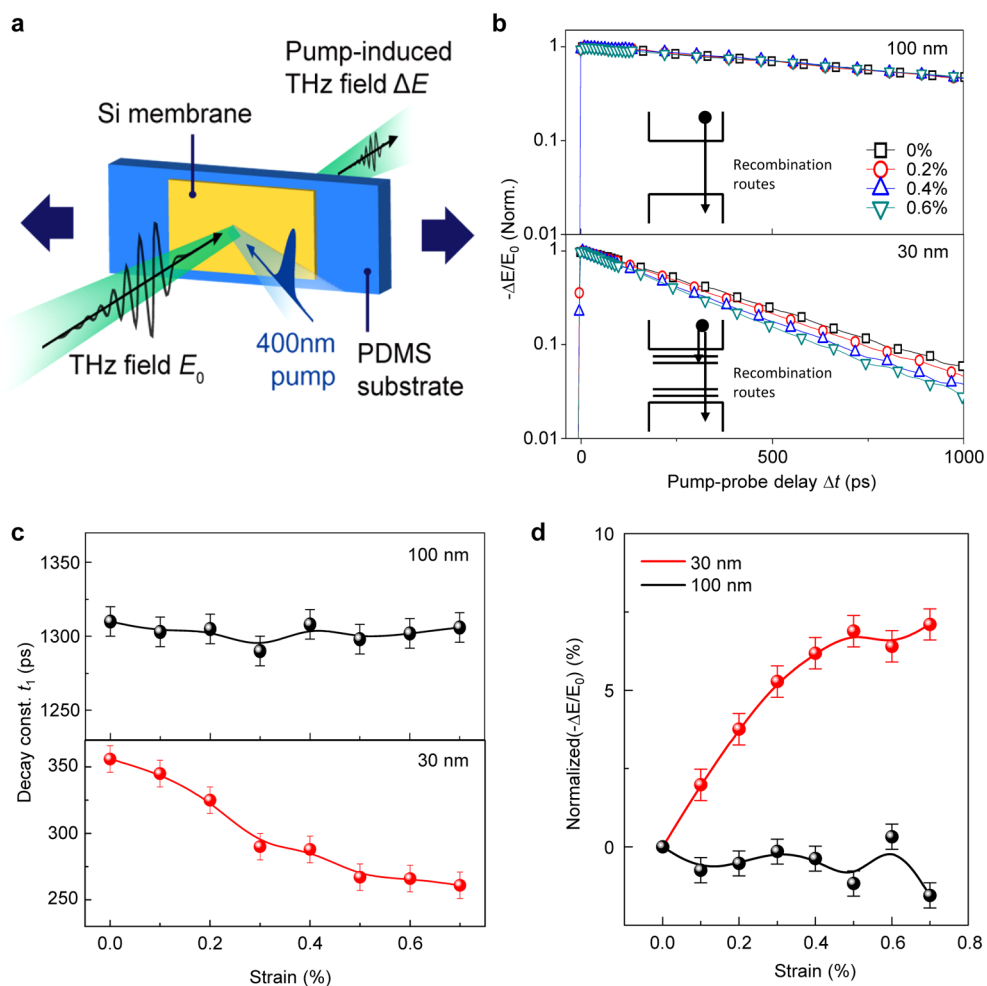


Figure 2. Carrier dynamics in Si NMs measured by ultrafast THz spectroscopy. (a) The schematic illustration of the measurement system, the 400 nm optical-pump laser, and the THz-probe focused on the Si NM, which is formed on the stretchable PDMS substrate. (b) The time-resolved THz peak dynamics in 100 nm (upper) and 30 nm (bottom) thick Si NM. The inset shows the schematic illustration of the mechanism and increase of recombination rate due to stress induced defect state. (c) The decay time constant to the monoexponential fitting from time-resolved data of panel b. We note that the error bars in all THz measurements indicate the standard deviation of recursive measurements at the same location on a sample. (d) The pump- and strain-induced THz peak changes as a function of strain, normalized by the THz peak change of 0% strain.

nm thick Si shows the well-known PZR behavior in which the sign is positive with a magnitude of $\sim 60 \times 10^{-11}/\text{Pa}$. However, the coefficient approached 0 for the 60 nm thick Si and a clear inverse PZR behavior with a negative sign of the coefficient was observed for the thin Si NMs with a thickness of less than 40 nm. The magnitude of the coefficient linearly increased as the thickness decreased. It was confirmed that the PZR behaviors in Si NMs are the actual PZR's by distinguishing the actual PZR from the pseudo PZR through resistance measurements with constant and stepped tensile strain as previous studies.⁵ The inset of Figure 1d shows the measured resistance of the 30 nm thick Si NMs in time with the stepped tensile strain of 0.3%. At the initial stage of the measurement, significant nonstress-related drift of resistance was observed, as reported in previous studies.^{5,8} However, in contrast to the previous reports the observed actual PZR and pseudo PZR showed clear differences with notable change in electrical resistance. The actual and pseudo PZR were clearly distinguished under a constant tensile strain with identical quantity of change in resistance with stepped-strain variations (Supporting Information Figure S2). It is notable that the resistance of Si NM decreases under tensile strain, while it increases in bulk Si, that is, the inverse

PZR measured in Si NM with a thickness of less than 40 nm is an actual PZR originating from the mechanical deformation. Although numerous investigations have been conducted to investigate the PZR in Si NMs,^{15–19} there are very limited quantities of studies reporting the inverse PZR.^{20–22} With the reference to prior reports, where the inverse PZR mainly arises from the carrier density variation (not from mobility of carriers), the optical absorption of the Si NMs were simply measured with the thickness of 30 nm under tensile strain to clarify the carrier density change of Si NMs. To avoid the change in incident angle of the light during measurement, we employed the Si NMs on stretchable polydimethylsiloxane (PDMS) substrate, instead of PET substrate. Figure 1e shows the optical absorption as a function of photon energy with different tensile strain from 0 to 0.6%. The absorption edge (optical band gap) is clearly red shifted with increasing strain, implying the strain-induced carrier density changes. We then estimate E_g considering the relationship of $\alpha \sim (\hbar\nu - E_g)^2$ for the indirect gap transition near the absorption edge²³ and summarized the E_g in the inset of Figure 1e as a function of strain. Here, it can be noted that the optical band gap is narrower when the strain is increased. This, in fact is one of the

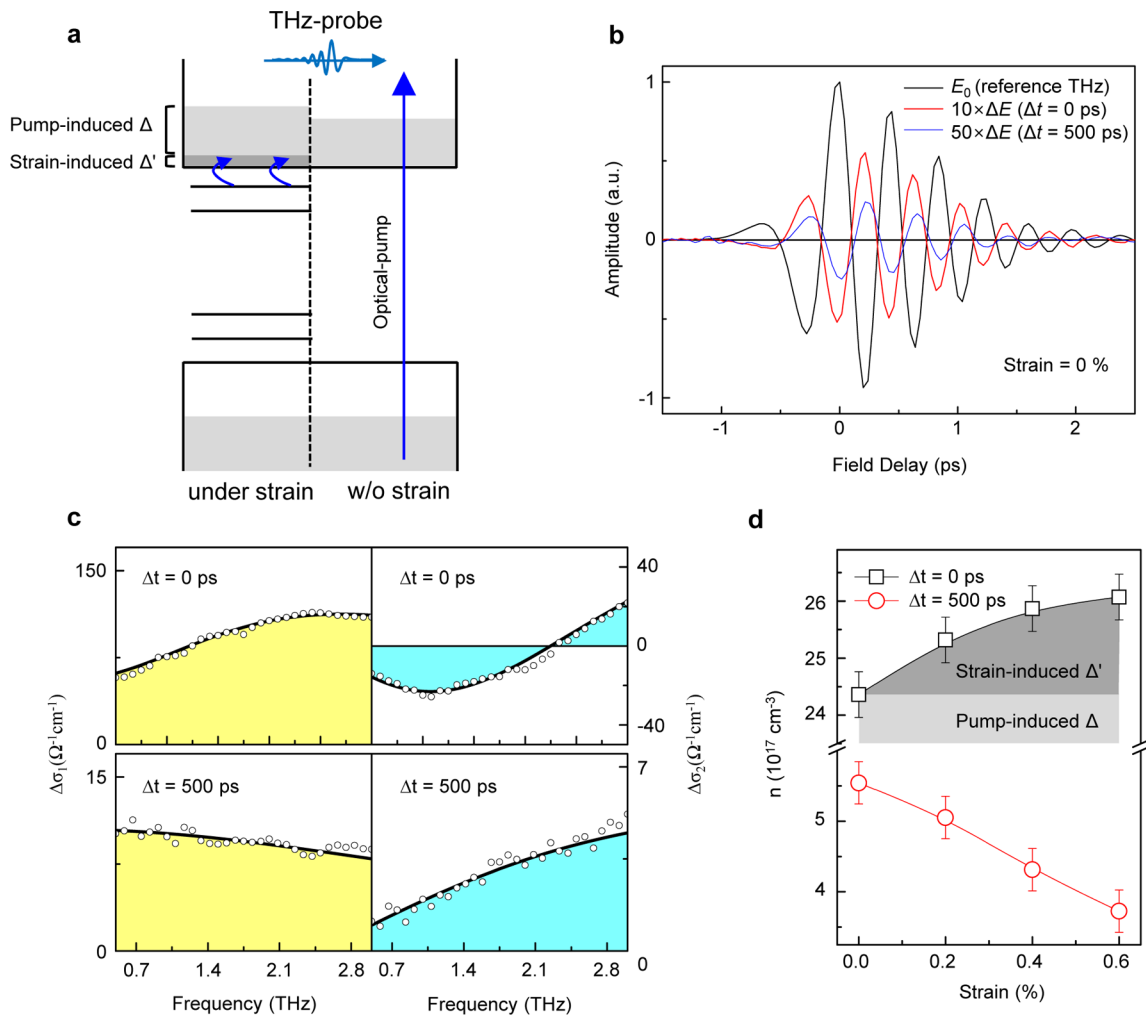


Figure 3. Evaluation of carrier concentration in Si NMs. (a) The schematic diagram of the THz spectral measurement on the band structure. The pump-induced carrier density and strain-induced carrier density are systematically illustrated by Δ and Δ' , respectively. (b) This panel displays the measured THz signals. Here, E_0 is the reference THz field without pump and ΔE is the pump-induced THz field change at $\Delta t = 0$ ps (red line) and $\Delta t = 500$ ps (blue line) under the applied strain of 0%. (c) The pump-induced complex conductivity changes (black dots) converted from the THz signals of panel b at $\Delta t = 0$ ps and $\Delta t = 500$ ps. The black lines display the model-based analysis. (d) The carrier density extracted from the modeling of panel c as a function of applied strain at $\Delta t = 0$ ps (black) and $\Delta t = 500$ ps (red).

well-established doping effects in Si, where the optical band gap is inversely proportional to the doping concentration above 10^{17} cm^{-3} .^{24,25}

The origin of optical band gap narrowing can be understood by reflecting on the strain-induced defect-state formation. When charge carriers are generated, for example, via optical absorption, the ground state is the defect state, not the conduction-valence band edge. For thin Si NMs, the defect state plays a more important role than what it does in the thick Si NMs. A more defect state means that there are new carrier recombination channels for the optically generated carriers, thereby, one can expect that carriers are recombined more rapidly compared to the thick sample.

To verify this idea, optical-pump THz-probe spectroscopy has been performed. Because THz spectroscopy is very sensitive to the free-carrier density and to the corresponding decay dynamics, the effect of defects on the carrier recombination can be determined. The schematic diagram of our THz experiment is shown in Figure 2a. When an ultrashort pump pulse with 400 nm center wavelength excites the Si NM, the pump-induced carrier dynamics with varying pump-probe

delay Δt is probed by THz probe pulse. Here, E_0 and ΔE refer to the THz field without pump and the pump-induced THz field change with pump, respectively. Figure 2b shows the normalized THz peak signals as a function of Δt . It can be seen that while the recombination dynamics of the 100 nm thick Si NM show a strain-independent behavior, the 30 nm thick Si NM exhibits a strong strain-dependent decay dynamics. For quantitative analysis, the time-resolved signals both for the 30 and the 100 nm thick Si NM are fitted by a monoexponential function $A \exp(-t/t_1)$. Because the carrier relaxation is strongly dependent to the defect density (see the illustrations in Figure 2b showing the defect-mediated recombination routes within band gap), the decay time constant t_1 should be faster due to a more defect state under tensile stress. Figure 2c shows the obtained t_1 for the 100 and 30 nm thick Si NMs. As expected, t_1 for the 100 nm thick Si NM is nearly constant with ~ 1300 ps regardless of the applied strain. For the 30 nm thick Si NM, however, t_1 gradually decreases from ~ 350 to 260 ps, indicating the defect state generation with applied strain. Figure 2d shows the normalized THz peak signals with increasing tensile strain; the data are normalized by the THz peak signal without strain.

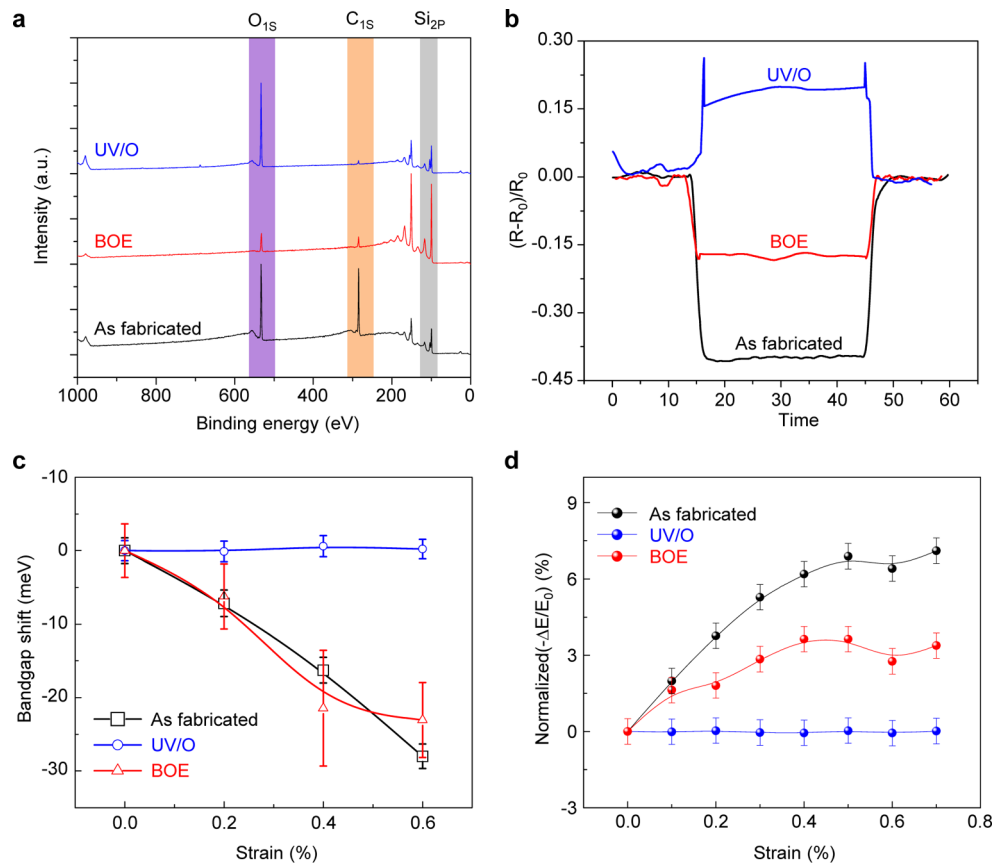


Figure 4. Dependency of PZR effect on surface state of Si NMs. (a) The XPS spectra of the sample with different surface, including UV/O-treated, BOE-treated, and as-fabricated surface. (b) The normalized resistance change of the Si NM with different surface states as a function of time. (c) The bandgap shift of the Si NM with different surface as a function of strain. The error bars indicate the fitted standard deviation of E_g . (d) The normalized change of the THz peak signal of 30 nm thick Si with different surface states as a function of strain.

The normalized $(-\Delta E/E_0)$ distinctively increases for the 30 nm thick Si NM, while that of the 100 nm thick Si NM is constant. Because the normalized THz peak signal is proportional to the total carrier density changes, the increased THz signals qualitatively reflects the increased carrier density. Because the optical excitation density is the same for all strain conditions, the increased carrier density can be properly attributed to the rise in strain-induced carrier density. This in fact well matches with the inverse PZR coefficient measured by the electric measurements (see Figure 1).

Now, the emerging concern is to determine the strain-induced increased carrier density. This can be done by examining the spectrally resolved THz conductivity. The low-energy nature of THz spectrum reflects the intraband conductivity, which can be integrated to determine the photoinduced carrier density. Figure 3a shows the schematic illustration of THz experiment to observe the carrier density changes in the Si NM band structure. Under tensile strain, the carrier density change is both caused by the pump-induced carrier density Δ and the strain-induced carrier density Δ' ; without strain, it is affected only by Δ . Figure 3b displays the measured E_0 and ΔE at $\Delta t = 0$ and 500 ps, when the pump fluence is $10 \mu\text{J}/\text{cm}^2$ and the applied strain is 0%. The sign of ΔE is the opposite of that of E_0 , implying the photoinduced transient absorption, that is, the increased carrier density. From the THz signals in Figure 3b, the frequency-dependent complex conductivity changes (black open dots) are obtained (Figure 3c), using a thin-film conductivity formula of $\Delta\sigma = -1/Z_0(\Delta E/$

$E_0)(n_s + 1)$, where Z_0 is the vacuum impedance and n_s is the PDMS substrate refractive index. For quantitative analysis, the measured conductivity data was modeled using the following Drude-Smith model²⁶

$$\Delta\sigma = \frac{\varepsilon_0\omega_p^2\tau}{(1 - i\omega\tau)} \left[1 + \frac{c}{(1 - i\omega\tau)} \right] \quad (2)$$

where ε_0 is the free-space permittivity, ω_p is the plasma frequency, τ is the scattering time, and c is the backscattering parameter. At $\Delta t = 0$ ps, $c = -0.75$ (when c equals -1 , it means a complete backscattering from the Si boundary), and $\tau = 0.05$ ps were obtained for all strain condition. The large backscattering value is understood as the carrier localization, which originates from the thickness-limited boundary of ultrathin Si and is enhanced under high carrier density.^{27,28} At $\Delta t = 500$ ps, $c = 0$ (which means the Drude-Smith backscattering model returns to the free-carrier Drude model) and $\tau = 0.04$ ps were obtained. The time-dependent conductivity changes (from carrier localization to free carrier) are associated with the time-dependent carrier recombination. As the photoinduced carrier density is decreased by Δt , c approaches 0 at $\Delta t = 500$ ps, and the corresponding THz conductivity becomes like that of the Drude free-carrier response because of the decreased carrier density compared to the response at $\Delta t = 0$ ps.²⁷ From the model parameter ω_p for each sample, the carrier density with increasing strain was extracted using the equation, $n = \varepsilon_0\omega_p^2 m^*/e^2$, where m^* is the effective mass of Si and e is the

elementary charge. The fitting results at different strain are displayed in Figure 3d and Supporting Information Figure S3. At $\Delta t = 0$ ps, the carrier density indeed rises with the increase of the tensile strain. This indicates that the carrier density change at each strain is governed by Δ' (not Δ), because the pump fluence is the same regardless of the applied strain. The obtained $\Delta' \sim 1.2 \times 10^{17} \text{ cm}^{-3}$ at strain 0.3% matches well with the value estimated from the electrical measurement. The carrier density at $\Delta t = 500$ ps, however, decreases as the tensile strain increases. This inverse behavior arises from the increased defect trapping, associated with defect-mediated recombination routes generated by the mechanical stress as illustrated in Figure 2b,c. Another important aspect of this THz analysis is that the mobility information can be obtained from the measured scattering time, that is, $\mu = e\tau/m^*$. While He et al. proposed that the mobility changes is the origin of the a-PZR effect,³ this paper's THz results show that the mobility is nearly constant with a value of $500 \pm 50 \text{ cm}^2/(\text{V}\cdot\text{s})$ for all strain conditions. Therefore, among the proposed possible origins of the inverse PZR effect, it can be seemingly elucidated that the carrier density change by the defect via applied tensile strain is the key mechanism in the ultrathin Si NMs.

Additionally, the phenomenon in different surface conditions was investigated, including as-fabricated, UV/O-treated, and BOE-treated surface, not only to control the inverse PZR behavior but also to clarify the location where the defect state arises. Figure 4a shows the X-ray photoelectron spectroscopy (XPS) spectra measured on the Si NMs with different surface states. It was ascertained that there is a strong carbon peak (which determined the carbon contamination) in the as-fabricated surface, and this peak disappears after UV/O treatment to cover surface with SiO_2 . Finally, samples where both SiO_2 and carbon were removed have been tested by BOE treatment to form clear bare Si surface. Figure 4b summarizes the measured PZR effects with various surfaces. The 30 nm thick Si NMs covered by SiO_2 show a positive PZR effect as previously reported.²⁰ However, the carbon-contaminated surface and bare Si surface show inverse PZR with a coefficient of $-76 \times 10^{-11}/\text{Pa}$ and $-35 \times 10^{-11}/\text{Pa}$, respectively. The different PZR behaviors from the various surfaces may be explained by the different energy states of the defects that arise under the tensile strain.^{29,30} To clarify, optical absorption measurements (which provide qualitative information on the carrier density changes) were performed, similar to the data in Figures 1 and 2. Figure 4c shows the bandgap shift of the Si NMs with different surface conditions. The significant bandgap narrowing effect is observed with the increasing tensile strain in the as-fabricated and the BOE-treated surface. For the UV/O-treated surface, no notable changes of the bandgap shift were observed, implying that the additional carrier only arises from the as-fabricated and BOE-treated surface. Because the defect state in the UV/O-treated surface cannot provide additional carriers, the PZR in the UV/O-treated Si NMs follows the conventional PZR of bulk Si. By utilizing the THz spectroscopy, the normalized $-\Delta E/E_0$ for samples were also measured with different surface conditions under tensile strain up to 0.7% (Figure 4d). The relative carrier density change in UV/O-treated surface shows negligible changes of THz signals, while as-fabricated and the BOE-treated surface show a significant positive correlation between the carrier density changes and the tensile strain. The relatively larger amount of carrier concentration changes that was observed in the as-fabricated surface compared to that of BOE-treated surface is in accord

with our electrical observation in Figure 4b. Consequently, the defect states mainly originate from the Si surface, such that the carrier-density-dominated PZR effect is controllable by simple surface treatment, similar to the mobility dominated PZR effect that was previously reported.³

Conclusions. In summary, this paper has investigated the inverse PZR in Si NMs with a thickness of less than 40 nm. The actual PZR is clearly distinguished from the pseudo PZR using a well-established electrical measurement of resistance in time as well as optical absorption spectroscopy. With the employment of the temporally and spectrally resolved THz spectroscopy, it has been shown and observed that the mechanism of the inverse PZR does not arise from the mobility changes but from the carrier concentration changes. By observing strain-dependent carrier decay dynamics, we concluded that the carrier density change is due to the defect-state formation induced by the applied strain. Furthermore, with the application of various surface-treatment conditions it has been clarified that the defect state mainly exists at the surface of the Si NMs. These results provide a promising route to control the carrier density dominated PZR effect by simple surface treatments. The insightful understanding for the inverse PZR is expected to offer a solid background for the integration of the nanostructured Si into novel nanoelectromechanical systems as well as flexible/stretchable Si electronics.

■ ASSOCIATED CONTENT

Supporting Information

Detailed materials and methods and supplementary figures. This material is available free of charge via the Internet at <http://pubs.acs.org>.

■ AUTHOR INFORMATION

Corresponding Authors

*E-mail: (J.-H.A.) ahnj@yonsei.ac.kr.

*E-mail: (H.C.) hychoi@yonsei.ac.kr.

Author Contributions

¹H.J. and J.K. contributed equally to this work.

Notes

The authors declare no competing financial interest.

■ ACKNOWLEDGMENTS

This work was supported by the National Research Foundation of Korea (NRF) grant funded by the Korea government (MSIP) (NRF-2012R1A2A1A03006049, NRF-2009-0083540, and NRF-2011-0013255), Global Frontier Program (2014M3A6B3063709) and the ICT R & D Program (Grant 10041066) funded by the Institute for Information & Communication Technology Promotion, Korea.

■ REFERENCES

- (1) Jang, H.; Lee, W.; Won, S. M.; Ryu, S. Y.; Lee, D.; Koo, J. B.; Ahn, S.-D.; Yang, C.-W.; Jo, M.-H.; Cho, J. H.; Rogers, J. A.; Ahn, J.-H. *Nano Lett.* **2013**, *13*, 5600–5607.
- (2) Ahn, J. H.; Kim, H. S.; Lee, K. J.; Zhu, Z. T.; Menard, E.; Nuzzo, R. G.; Rogers, J. A. *IEEE Electron Device Lett.* **2006**, *27*, 460–462.
- (3) He, R.; Yang, P. *Nat. Nanotechnol.* **2006**, *1*, 42–46.
- (4) Rowe, A. C. H. *Nat. Nanotechnol.* **2008**, *3*, 311–312.
- (5) Milne, J. S.; Rowe, A. C. H.; Arscott, S.; Renner, C. *Phys. Rev. Lett.* **2010**, *105*, 226802.
- (6) Yang, Y.; Li, X. *IEEE Int. Conf. Micro Electro Mech. Syst., Tech. Digest* **2009**, 555.
- (7) Yang, Y.; Li, X. *IEEE Electron Device Lett.* **2011**, *32*, 411–413.

- (8) Rowe, A. C. H. *J. Mater. Res.* **2014**, *29*, 731–744.
- (9) Smith, C. S. *Phys. Rev. Lett.* **1954**, *94*, 42.
- (10) Caughey, D. M.; Thomas, R. E. *Proc. IEEE* **1967**, *55*, 2192–2193.
- (11) Joyce, H. J.; Wong-Leung, J.; Yong, C.-K.; Docherty, C. J.; Paiman, S.; Gao, Q.; Tan, H. H.; Jagadish, C.; Lloyd-Hughes, J.; Herz, L. M.; Johnston, M. B. *Nano Lett.* **2012**, *12*, 5325–5330.
- (12) Kim, J.; Oh, J.; In, C.; Lee, Y. S.; Norris, T. B.; Jun, S. C.; Choi, H. *ACS Nano* **2014**, *8*, 2486–2494.
- (13) Strait, J. H.; George, P. A.; Levendorf, M.; Blood-Forsythe, M.; Rana, F.; Park, J. *Nano Lett.* **2009**, *9*, 2967–2972.
- (14) Suo, Z.; Ma, E. Y.; Gleskova, H.; Wagner, S. *Appl. Phys. Lett.* **1999**, *74*, 1177.
- (15) Toriyama, T.; Funai, D.; Sugiyama, S. *J. Appl. Phys.* **2003**, *93*, 561–565.
- (16) Reck, K.; Richter, J.; Hansen, O.; Thomsen, E. V. *Proc. IEEE MEMS* **2008**, 717–720.
- (17) Koumela, A.; Mercier, D.; Dupre, C.; Jourdan, G.; Marcoux, C.; Ollier, E.; Purcell, S. T.; Duraffourg, L. *Nanotechnology* **2011**, *22*, 395701.
- (18) Barwicz, T.; Klein, L.; Koester, S. J.; Hamann, H. *Appl. Phys. Lett.* **2010**, *97*, 023110.
- (19) Neuzil, P.; Wong, C. C.; Reboud, J. *Nano Lett.* **2010**, *10*, 1248–1252.
- (20) Yang, Y.; Li, X. *Nanotechnology* **2011**, *22*, 015501.
- (21) Yong, Z.; Xinyu, L.; Changhai, R.; Yan Liang, Z.; Lixin, D.; Yu, S. *J. Microelectromech. Syst.* **2011**, *20*, 959–967.
- (22) Lugstein, A.; Steinmair, M.; Steiger, A.; Kosina, H.; Bertagnolli, E. *Nano Lett.* **2010**, *10*, 3204–3208.
- (23) Mark, F. In *Optical properties of solids*, 2nd ed.; Oxford University Press: Oxford, 2010; p 80.
- (24) Lanyon, H. P. D.; Tuft, R. A. *IEEE Trans. Electron Devices* **1979**, *26*, 1014–1018.
- (25) Slotboom, J. W.; de Graaff, H. C. *Solid-State Electron.* **1976**, *19*, 857–862.
- (26) Smith, N. V. *Phys. Rev. B* **2001**, *64*, 155106.
- (27) Li, G. F.; Li, D.; Jin, Z. M.; Ma, G. H. *Opt. Commun.* **2012**, *285*, 4102–4106.
- (28) Walther, M.; Cooke, D. G.; Sherstan, C.; Hajar, M.; Freeman, M. R.; Hegmann, F. A. *Phys. Rev. B* **2007**, *76*, 125408.
- (29) Agostinelli, G.; Delabie, A.; Vitanov, P.; Alexieva, Z.; Dekkers, H.; De Wolf, S.; Beaucarne, G. *Sol. Energy Mater. Sol. Cells* **2006**, *90*, 3438–3443.
- (30) Fahey, P. M.; Griffin, P.; Plummer, J. *Rev. Mod. Phys.* **1989**, *61*, 289.